IEEE Robotics and Automation Letters (RA-L) paper, presented at ICRA 2024, Yokohama, Japan. Cite as RA-L paper.

Design of a Deployable Continuum Robot Using Elastic Kirigami-Origami

Yunong Li, Hailin Huang, and Bing Li, *Senior Member, IEEE*

***Abstract*—Inspired by Yoshimura origami, this study presents a novel deployable modular continuum robot that achieves configuration maintenance by utilizing active cables and passive elastic deformation of kirigami-origami. In this study, the synchronous motion of each module is improved by using slider-crank mechanisms. Using screw theory, the comprehensive kinematics of the proposed deployable kirigami-origami robot were analyzed, explaining how elastic restoring force is generated in each module. A physical prototype was developed, and the performance of this origami-inspired continuum robot was evaluated by comparing the motion properties of the proposed robot with the robot without elastic rings and synchronism mechanisms. Besides, position accuracy, trajectory tracking ability, stiffness, and load capacity experiments were also conducted. By integrating a pneumatic soft hand at the end of the proposed robot, an object-grasping experiment was conducted to verify the feasibility.**

***Index Terms*—Mechanism design, kinematics, origami continuum robot, kirigami-origami.**

I. Introduction

CONTINUUM robots have become a hot topic in robotics over the past few decades due to their lightweight constructions, unique flexible motions, and integrated actuation. They hold enormous potential for various applications, including space exploration [1], underwater research [2], minimally invasive surgery [3], etc. These robots can be actuated in several ways, including cable-driven [4], [5], pneumatic-driven [6], [7], and hybrid-driven [8], [9]. Among these options, cable-driven continuum robots stand out due to their ease of fabrication and high control precision, which has garnered significant interest among researchers.

Most traditional continuum robots are undeployable, which restricts the possibility of elaborate applications. Many researchers have dedicated themselves to using soft pneumatic actuators to achieve such tasks. However, in most cases, these designs have small deploy/fold ratios. Fortunately, origami art can provide a new perspective for achieving structural deployment by incorporating special origami creases on planar material [10], [11]. Some interesting results have been achieved in these fields, such as mobile robots [12], [13], proprioceptive actuators [14], artificial muscles [15], adaptive solar radiation-reducing facades [16], inflatable metamorphic origami [17], etc.

Yoshimura origami has been widely used due to its ability to accomplish extending motion and bi-directional motion with a compact folded configuration. Yunti Xu et al. [18] employed a hydro-fold mechanism to simplify fabrication steps and create the main body of an origami continuum robot. Junius Santoso et al. [19] integrated the actuation onto a circuit board installed at the bottom of each modular origami. Inspired by annelids, Xianhe Wei et al. [20] proposed a four-section continuum robot made of origami and kirigami. Haitong Liang et al. [21] designed a modified Yoshimura origami unit that owns an extra degree along the axial direction and proposed a three-unit continuum robot. Jingyu Zhang et al. [22] created an origami continuum robot, calculated its kinematic model, and controlled its trajectory by using a motion capture system. Due to the tube structure of Yoshimura origami, configuration maintenance of these designs often relied on the elasticity of creases or materials. Because the elasticity of origami materials could not provide enough stiffness, it is challenging for those robots to maintain their configuration when performing specific tasks, especially for the deployment motion to reach a large working space.

To address the issue, several works have been conducted. Salerno et al. [23] introduced a Kresling origami on a Yoshimura unit and incorporated shape memory alloy (SMA) springs to improve performance. Robertson et al. [24] affixed three pouch motors on the top of an origami unit to maintain its configuration. Liu et al. [25] took inspiration from otariidae flippers and proposed an auxiliary arm driven by air. Silicone origami air chambers and kirigami restraint layers were used for deploying and pre-designed bending motions. Zhang et al. [26] employed hybrid actuation, using cables as geometric constraints to control motions and a pneumatic system to maintain configuration and adjust stiffness. Yu et al. [27] devised an origami mortise-tendon structure that could achieve both compliance and elasticity,

Manuscript received 1 July 2023; accepted 18 October 2023. Date of publication 3 November 2023; date of current version 9 November 2023. This letter was recommended for publication by Associate Editor Y. She and Editor L. Pallottino upon evaluation of the reviewers' comments. This work was supported in part by the National Natural Science Foundation of China under Grant 52075113, in part by Shenzhen Peacock Innovation Team Project under Grant KQTD20210811090146075, in part by Shenzhen Science and Technology Program under Grant JCYJ20210324115-811033, and in part by Shenzhen Natural Science Fund under Grant GXWD20220811151529003. *(Corresponding author: Hailin Huang.)*

Yunong Li is with the School of Mechanical Engineering and Automation, Harbin Institute of Technology, Shenzhen 518052, China (e-mail: yunongli@foxmail.com).

Hailin Huang and Bing Li are with the School of Mechanical Engineering and Automation, Harbin Institute of Technology, Shenzhen 518052, China, and with the Guangdong Provincial Key Laboratory of Intelligent Morphing Mechanisms and Adaptive Robotics, Harbin Institute of Technology, Shenzhen 518052, China, and also with the State Key Laboratory of Robotics and System, Harbin Institute of Technology, Harbin 150001, China (e-mail: huanghailin@hit.edu.cn; libing.sgs@hit.edu.cn).

This letter has supplementary downloadable material available at https://doi.org/10.1109/LRA.2023.3330055, provided by the authors.

Digital Object Identifier 10.1109/LRA.2023.3330055

IEEE Robotics and Automation Letters (RA-L) paper, presented at ICRA 2024, Yokohama, Japan. Cite as RA-L paper.

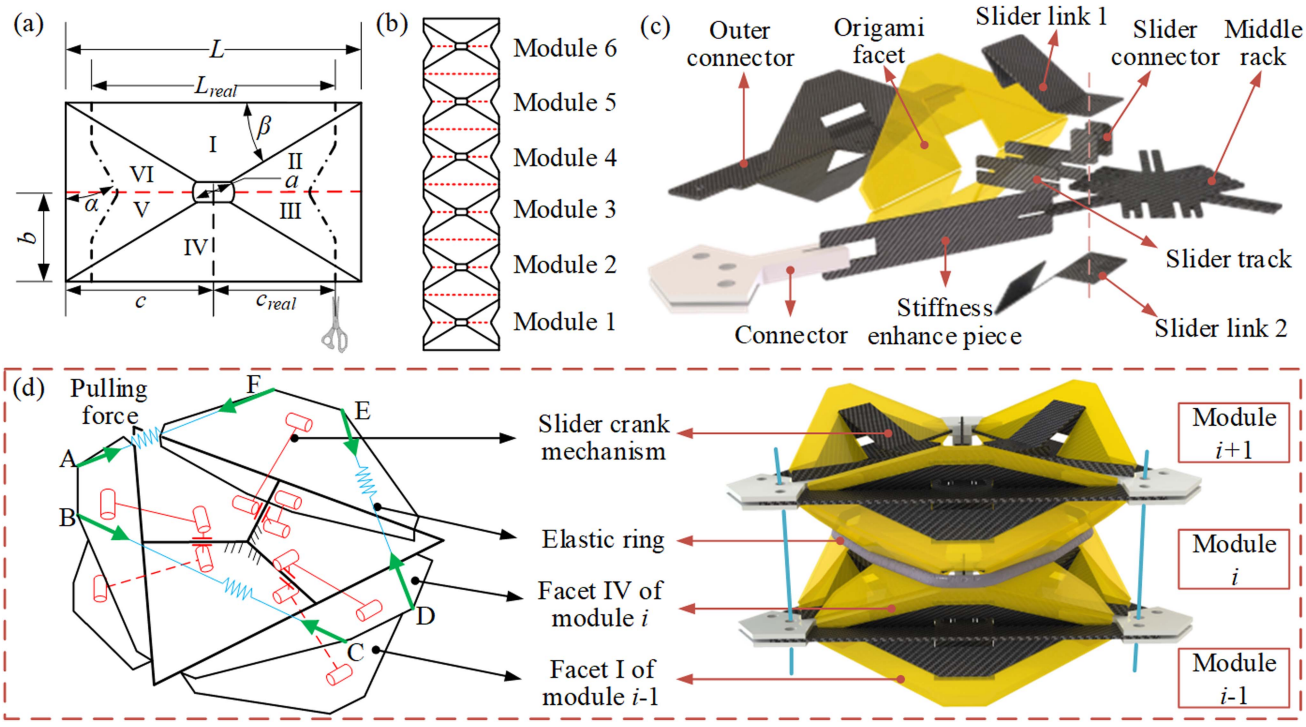

Fig. 1. Design of the proposed robot. (a) Basic kirigami unit. (b) Kirigami chain. (c) Explosion view of the synchronism mechanism. (d) The kirigami-origami module with elastic ring.

though the proposed robot forfeited its deployable capability. Zhuang et al. [28] employed conventional springs to maintain the configuration of the robot and used SMA springs to actuate the end origami unit independently. Most of these studies utilized springs between origami units or extra driving systems to enhance configuration maintenance ability, resulting in a significant reduction in folding ratio, which is the most fascinating property of origami structures. Additionally, an issue that has been overlooked by most of the above-mentioned research is the motion synchronism between origami modules, which means the configuration consistency of each module when the robot is moving. As each Yoshimura origami module can be deemed as a parallel mechanism with 3 degrees of freedom (DoFs), for an n-unit continuum robot, the theoretical DoFs are $3n$, which would require $3n$ actuators to completely control the entire configuration. Embedding so many actuators is impractical, so a common solution is to divide the structure into 2 or 3 sections and actuate these sections separately. This means that the origami units in the middle, between both ends, cannot be fully constrained by cables. Such under actuation leads to mutable configurations and motion uncertainty in the robot.

In summary, current origami continuum robots are facing two contradictory challenges: how to increase the deploy/fold ratio and how to improve synchronicity. In response to these challenges, this letter proposes a novel kirigami-origami-inspired self-deployable continuum robot with a high deploy/fold ratio considering the motion synchronicity in each module. This study analyzes the mobility and the kinematic model of the robot, followed by a detailed analysis of the principle of elastic restoring force generation for configuration maintenance. Experiments were also conducted to test the performance of the robot. The main contributions of this study include:

- A novel deployable continuum robot using elastic kirigami-origami was proposed, which can maintain the configuration by using active cables and passive elasticity of the kirigami-origami module.
- A new slider-crank mechanism is designed to improve the motion synchronicity of each module while avoiding singularity caused by elastic force.
- A comprehensive kinematic model for describing the Yoshimura kirigami-origami module is proposed, which illustrates the reason why the robot can achieve self-deployment by using elastic rings.

II. Design and Mobility Analysis of the Robot

A. Overall Structure Design

The notations of the kirigami unit based on Yoshimura origami pattern are shown in Fig. 1(a). The kirigami unit consists of six creases and six facets (I, II, III, IV, V, and VI). The dash lines denote valley creases, the solid lines denote mountain creases, the dash-dotted lines correspond to the cut margin of the kirigami unit, and the continuous lines outside represent the initial region of the Yoshimura pattern. Considering the thickness of the origami, a hole of diameter a is cut off at the intersection point of the six creases such that the structure can be fully folded. In this design, L and L_{real} are 60 mm and 50 mm respectively, $\alpha = 30°$,$\beta = 31°$. These design parameters are determined by the fabrication condition, and other parameters can be calculated

accordingly. The whole structure of the proposed robot has three kirigami chains with six kirigami units, as depicted in Fig. 1(b). Three kirigami chains are connected by five proposed mechanisms to form a triangular-prism-shaped structure for the deployable continuum robot, and Fig. 1(c) shows the explosion view of one synchronism mechanism.

In a synchronism mechanism, there are three slider crank mechanisms, one of which is used to connect facet IV of the module i and facet I of the module $i-1$. Each slider consists of two synchronous cranks, ensuring that the driving angles between two adjacent modules are identical, so the configuration of each module is also theoretically identical. By attaching an elastic ring to the cupped region of each module, the elastic restoring force is generated while the module changes from its initial state. The pulling force of the elastic ring can shorten the distances BC, DE, and FA to pull the origami in the deployed configuration, as shown in Fig. 1(d), and the driving cables can pull the origami in the opposite configuration through the folding motion. The folding motion will have to overcome the pulling force of the elastic ring to lengthen the distances BC, DE, and FA. During this period, the slider-crank mechanism is passively driven.

The proposed robot comprises six different parts: the outer connector, slider, middle rack, stiffness enhance piece, assembly connector, and elastic ring, as depicted in Fig. 1(c) and (d). The outer connector is fixed in a designated space on the exterior origami structure, providing a location for the assembly of three kirigami chains and internal components. The slider contains two links and two slider connectors, with the connectors controlling the height of the slider. Two links, slider link 1 and slider link 2, are bonded to the inner side of the kirigami-origami structure, as shown in Fig. 1(c). The middle rack is used to fix stiffness enhance pieces and slider tracks, limiting their travel in case of singularity due to elastic forces. Taking advantage of material anisotropy, stiffness enhance pieces can maintain the relative position of the structure with high stiffness. A 3D-printed assembly connector is employed to fix the outer connector and the stiffness enhance pieces, forming the complete structure with the use of bolts. Finally, elastic rings, made of rubber, are tied to the middle creases of each module.

B. Mobility Analysis

The proposed robot can be deemed as a combination of six kirigami-oigami modules. The Yoshimura kirigami-origami module of the proposed robot can be regarded as a 3-RSR parallel mechanism [29], where each origami chain consists of two revolute joints and a spherical joint. The schematic diagram of the kirigami module and equivalent parallel mechanism is shown in Fig. 2(a). The intersection points of all six creases of the basic kirigami unit (the spherical center of the spherical joint) are represented by $B_i(i=1,2,3)$ and the corresponding chain is denoted by chain i. For the sake of convenience in subsequent analysis, a base coordinate system $\{O_b\}$ is established at the geometric center of the lower regular triangle $C_1C_2C_3$. The x-axis points from O_b to C_1, the z-axis is perpendicular to plane C, and the y-axis is consistent with the right-hand rule. Based

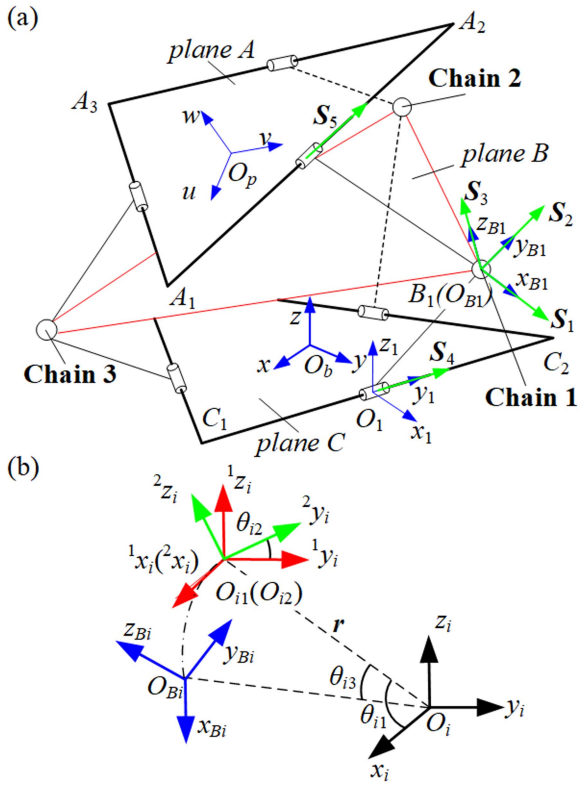

Fig. 2. Simplified model of the Yoshimura kirigami-origami module. (a) Equivalent mechanism. (b) Transformation relationships of chain coordinate systems.

on the Grübler-Kutzbach formula, the DoFs of the Yoshimura kirigami-origami module can be calculated as follows:

$$M = d(n-g-1)+\sum_{i=1}^{g} f_i + v - \xi = 6(8-9-1)+15 = 3 \tag{1}$$

where d is the order of the mechanism, n is the number of moving parts, g is the number of joints, f_i is the degrees of freedom of joint i, v and ξ are the number of redundant constraints and virtual constraints respectively.

As the number of kirigami modules increases, the total DoFs will also increase. However, by using the synchronism mechanism, the robot can maintain an identical deployment between two adjacent modules, resulting in two adjacent modules having the same configuration, and the robot also has 3 DOFs regardless of the number of modules.

III. Kinematic Modeling and Analysis

A. Forward Kinematics

Based on previous analysis, the robot has three DOFs, which implies that the deformation of each module is identical. Thus, it is reasonable to assume that the end pose is the superposition of six modules. The configuration of a classical Yoshimura kirigami-origami module can be simplified as illustrated in Fig. 3. Let the cable lengths of A_1C_1, A_2C_2 and A_3C_3 be denoted as l_1, l_2 and l_3 respectively. By driving the three cables, the module could be controlled.

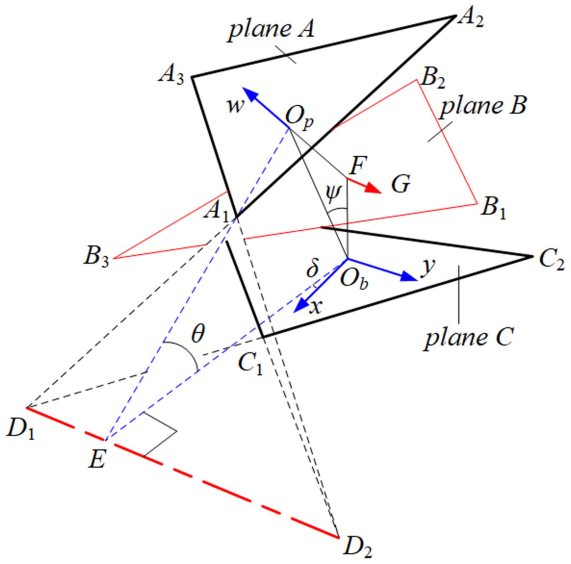

Fig. 3. Configuration description of a Yoshimura kirigami-origami module.

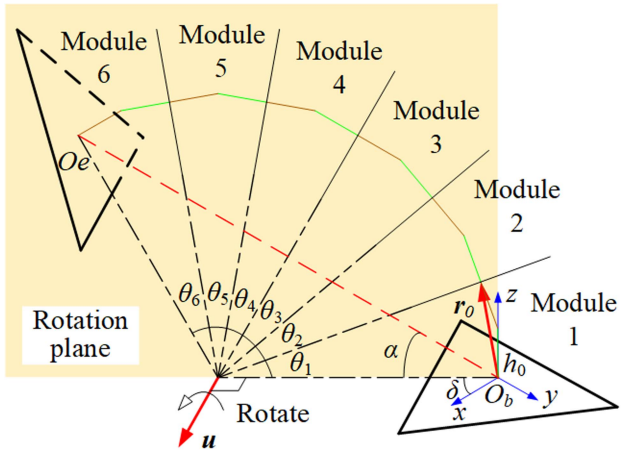

Fig. 4. Equivalent motion description of six-module kirigami-origami robot used for inverse kinematics.

The origin of the body-fitted coordinate system $\{O_p\}$ is located at the geometric center of regular triangular $A_1A_2A_3$. The u axis points from O_p to A_1, and the w axis is vertical to plane A, pointing upwards. The v-axis follows the right-hand rule. In general, plane A and plane B intersect along line D_1D_2. A perpendicular line from O_b intersects D_1D_2 at point E. Connecting E and O_p, the angle between EO_b and EO_p is denoted as θ. So plane A can be regarded as rotating by θ degrees around axis D_1D_2 from plane C [30]. It is ambiguous to describe the actual rotation axis D_1D_2 in $\{O_b\}$, so let axis z intersect plane B at point F, and make a unit vector $\boldsymbol{FG}$ parallel to D_1D_2. The position of plane A can be obtained through two sequential transformations.

Assuming that the moving plane A is initially coincident with plane C, the first transformation translates with distance h towards the positive direction of the z axis. The second transformation rotates plane A by θ degrees about the virtual axis FG. By employing the product of the exponential (POE), once we obtain the screw axis $\boldsymbol{S}_1$, $\boldsymbol{S}_2$, and the relative h, θ of the above two transformations, we can determine the position and orientation of plane A:

$$\boldsymbol{T}_{\text{unit}} = \boldsymbol{T}_2\boldsymbol{T}_1 = e^{[\boldsymbol{S}_2]_\times\theta}e^{[\boldsymbol{S}_1]_\times h} \tag{2}$$

Let δ denotes the angle between O_bE and the positive direction of the x axis to describe the orientation of $\boldsymbol{FG}$, and r denotes the apothem of plane A. The length of line O_bF is h_0, and thus the distance of h is equal to $2h_0$. The angle between O_bO_p and the z axis is denoted by ψ, and hence, θ is equal to 2ψ, because O_pFO_b is an isosceles triangle. Let vector $\boldsymbol{O_bO_p}$ be denoted by $\boldsymbol{r}_0$ with a length of r_0. Accordingly, $2h_0$ can be expressed as $r_0/\cos(\psi)$. The screw axes of the two transformations can be obtained accordingly:

$$\begin{aligned}\boldsymbol{S}_1 &= [0\ \ 0\ \ 0\ \ 0\ \ 0\ \ 1]^{\boldsymbol{T}}\\ \boldsymbol{S}_2 &= \left[-\sin\delta\ \ \cos\delta\ \ 0\ \ -\tfrac{r_0\cos\delta}{2\cos\psi}\ \ -\tfrac{r_0\sin\delta}{2\cos\psi}\ \ 0\right]^T\end{aligned} \tag{3}$$

The relationships between these cable lengths and other parameters can be obtained from geometry, and the detailed derivation can be seen from supplementary material. From (2) and (3) we can get the end pose of a module in the form of a 4×4 homogeneous transformation matrix $\boldsymbol{T}_{unit\_i}$, where i represents the i_{th} module in the whole continuum robot. The end pose of the robot with n modules:

$$\begin{aligned}\boldsymbol{T}_{unit\_1} = \boldsymbol{T}_{unit\_2} = \cdots = \boldsymbol{T}_{unit\_n} = \boldsymbol{T}_{unit}(l_1, l_2, l_3)\\ \boldsymbol{T} = \boldsymbol{T}_{unit\_1}\boldsymbol{T}_{unit\_2}\cdots\boldsymbol{T}_{unit\_n-1}\boldsymbol{T}_{unit\_n}\end{aligned} \tag{4}$$

where $\boldsymbol{T}_{unit}(l_1, l_2, l_3)$ means a simplified notation of forward kinematics function, the variables are cable lengths of a kirigami-origami module, so the total lengths of three driving cables are nl_1, nl_2, nl_3, respectively. The forward kinematics will be verified in subsection B of Section V.

B. Inverse Kinematics

The configuration of a kirigami-origami module can be simplified as a combination of two rigid rods, namely, O_bF and O_pF, as illustrated in Fig. 3. The overall deformation can then be conceptualized as a series of rigid rods whose lengths vary at different configurations, as depicted in Fig. 4.

O_e represents the end of the robot, l denotes the distance between O_e and O_b, $\boldsymbol{u}$ is a unit vector utilized to describe the direction of the rotation axis, and α represents the angle between O_eO_b and O_bE. Geometrically, we can derive the following relationship:

$$\alpha = \sin^{-1}\left(\frac{O_{e,z}}{\sqrt{O'_e\cdot O_e}}\right)\quad \theta = \frac{180^\circ - 2\alpha}{6} = 2\psi \tag{5}$$

From (5), the rotation angle of one module can be solved. Therefore, the only remaining task is to determine the values of the unit vectors $\boldsymbol{u}$ and $\boldsymbol{r}_0$. It is easy to get:

$$\begin{aligned}\sin\delta = \frac{O_{e,y}}{\sqrt{O_{e,x}^2+O_{e,y}^2}}\quad \cos\delta = \frac{O_{e,x}}{\sqrt{O_{e,x}^2+O_{e,y}^2}}\\ \boldsymbol{u} = [-\sin\delta, \cos\delta, 0]^{\boldsymbol{T}}\end{aligned} \tag{6}$$

where $O_{e,x}$ and $O_{e,y}$ mean the corresponding coordinates of O_e. According to Rodrigües rotation formula:

$$\boldsymbol{R} = \mathbf{I}_{3\times3} + \sin\theta \times [\boldsymbol{u}]_\times + (1-\cos\theta) \times [\boldsymbol{u}]_\times \times [\boldsymbol{u}]_\times \quad (7)$$

where $[\boldsymbol{u}]_\times$ represents the skew-symmetric matrix of the vector $\boldsymbol{u}$. Substituting (5) and (6) into (7), the rotation matrix of one module's moving plate can be obtained. The description of vector $\boldsymbol{r}_0$ can be solved as follows:

$$\begin{aligned} \|r_0\| &= \tfrac{l}{2\cos\alpha}\sin\psi \times 2 = \tfrac{l\sin\psi}{\cos\alpha} \\ \boldsymbol{r}_0 &= [\|r_0\|\sin\psi\cos\delta, \|r_0\|\sin\psi\sin\delta, \|r_0\|\cos\psi]^{\boldsymbol{T}} \end{aligned} \quad (8)$$

Based on the calculations, we can get the homogeneous transformation matrix $\boldsymbol{T}_{unit\_i}$ and the relative coordinate $A_i(i=1,2,3)$ of a kirigami-origami module:

$$\boldsymbol{T}_{unit\_i} = \begin{bmatrix} \boldsymbol{R} & \boldsymbol{r}_0 \\ \boldsymbol{0} & 1 \end{bmatrix} \quad \boldsymbol{A}_i = \boldsymbol{T}_{unit\_i} \times \boldsymbol{C}_i \quad (9)$$

where $C_i(i=1,2,3)$ is the position vector of point C_i. So the cable lengths of an n-module continuum robot $nl_i(i=1,2,3)$ are:

$$nl_i = n\sqrt{(\boldsymbol{A}_i - \boldsymbol{C}_i)\cdot(\boldsymbol{A}_i - \boldsymbol{C}_i)} \quad (10)$$

Experiments will be conducted to verify the inverse kinematics in Section B of Section V.

IV. Self-Deployment Principle

A. Module Branch Chain Description

To illustrate how elastic rings generate restoring force for origami modules, it is necessary to provide an accurate position and orientation description of the three branch chains in a module. For ease of expression, three fixed coordinate systems $\{O_i\}(i=1,2,3)$ were introduced, the origin of each located in the middle point of C_1C_2, C_2C_3, and C_3C_1, respectively. The $x_{Bi}-O_{Bi}-y_{Bi}$ planes of these coordinate systems are coincident with plane B, where x_{Bi} is pointing outward and perpendicular to the corresponding edge, as presented in Fig. 2(a).

For chain 1, once the relationships between $\{O_{Bi}\}$ and $\{O_b\}$ are established, the pose of the branch chain can be obtained. The transformation from $\{O_b\}$ to $\{O_i\}$ is easy to get, so the main target is to get the transformation from $\{O_i\}$ to $\{O_{Bi}\}$. There is no rotation mobility along the z axis due to geometric constraints of the kirigami-origami, and the DOFs of the module is three. So $\{O_{Bi}\}$ can be obtained from$\{O_i\}$ after three transformations, as shown in Fig. 2(b). First, transform $\boldsymbol{r} = [b\cos(\theta_{i1}), 0, b\sin(\theta_{i1})]^{\boldsymbol{T}}$ from $\{O_i\}$ to $\{O_{i1}\}$, where $\boldsymbol{r}$ represents the vector points from origin of $\{O_i\}$ to origin of $\{O_{i1}\}$. Second, $\{O_{i1}\}$ is rotated by an angle of θ_{i2} around the ${}^1x_i$ axis to obtain $\{O_{i2}\}$. Finally, $\{O_{i2}\}$ is rotated by an angle of θ_{i3} around the y_i axis of $\{O_i\}$ to obtain $\{O_{Bi}\}$. Because $\{O_{i1}\}$ and $\{O_{i2}\}$ only represent the middle states of the final transformation, they are only shown in Fig. 2(b). By following these steps, we can determine the configuration of the branch chain. From geometry we have:

$$\theta_{i2} = \arcsin\left(\frac{l_{i+1}-l_i}{2L}\right) \quad \theta_{i1} = \arcsin\left(\frac{l_i+l_{i+1}}{4b\cos\theta_{i2}}\right) \quad (11)$$

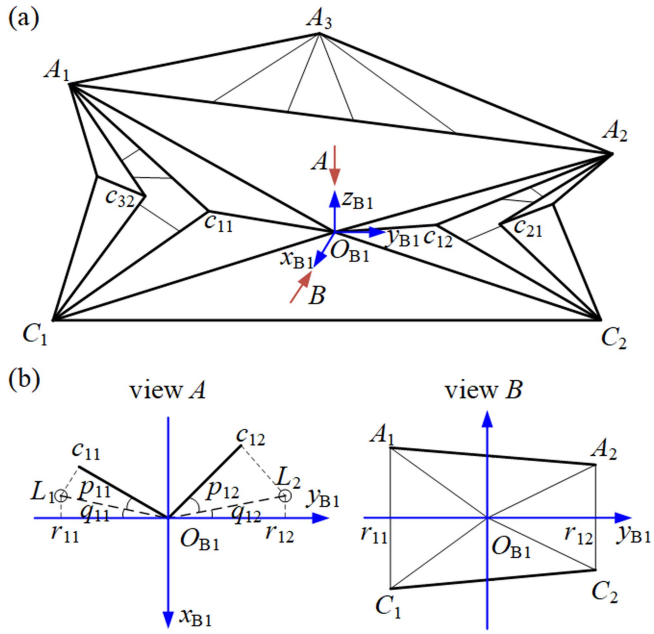

Fig. 5. Facets of module branch chain 1. (a) Geometry relationships of module branch chain 1. (b) Two views of branch chain 1.

It is complex to calculate θ_{i3} because the coordinate of A_i in $\{O_b\}$ is required. Based on forward kinematics and geometry we have:

$$\begin{aligned} {}^{O_i}A_i &= {}^{O_b}\boldsymbol{T}_{O_i}^{-1} \times {}^{O_b}A_i \\ \theta_{i3} &= \arcsin\left(\frac{{}^{O_i}A_{i,x}}{\|{}^{O_i}A_i\|}\right) \end{aligned} \quad (12)$$

where ${}^{O_i}A_i$ represents the coordinate of A_i in $\{O_i\}$, ${}^{O_i}A_{i,x}$ represents the x component of ${}^{O_i}A_i$. ${}^{O_b}\boldsymbol{T}_{O_i}^{-1}$ represents the inverse homogeneous transformation matrix from $\{O_b\}$ to $\{O_i\}$. ${}^{O_b}A_i$ is the coordinate of A_i in $\{O_b\}$ which can be obtained from forward kinematics. According to (11) and (12), the pose of the module branch chain can be described as the homogenous transformation matrix from $\{O_b\}$ to $\{O_{Bi}\}$, which can be expressed as:

$${}^{O_b}\boldsymbol{T}_{O_{Bi}} = {}^{O_b}\boldsymbol{T}_{O_i}\mathbf{Rot}(y,\theta_{i3})\,\mathbf{Trans}(\boldsymbol{r})\,\mathbf{Rot}(x,\theta_{i2}) \quad (13)$$

B. Restoring Force Generation Analysis

Fig. 5(a) shows the diagram of a kirigami-origami module, and Fig. 5(b) provides a more detailed diagram from two different views. c_{11} and c_{12} are in the negative part of y_{B1} and positive part of y_{B1}, respectively. c_{i1} and $c_{i2}(i=1,2,3)$ are used to represent the corresponding points on other chains. c_{11} and c_{12} are coincident with the $x_{B1}-O_{B1}-y_{B1}$ plane. Moreover, plane $A_1A_2C_1C_2$ is consistently parallel to plane $y_{B1}-O_{B1}-z_{B1}$. The points where actuation cables l_1 and l_2 intersect to plane $x_{B1}-O_{B1}-y_{B1}$ are denoted as L_1 and L_2, respectively. The intersection points of the y axis and the projection lines of l_1 and l_2 are represented by r_{11} and r_{12}, respectively.

The positions of c_{11} and c_{12} are described by the angles p_{11}, p_{12}, q_{11} and q_{12}, which can be calculated as follows:

$$\begin{aligned} p_{1j} &= \arctan\left(\frac{b\cos\theta_{11}}{\sqrt{c^2+(b\sin\theta_{11})^2-l_j^2/4}}\right) \\ q_{1j} &= \arccos\left(\frac{2d^2-2b^2}{\sqrt{(d^2-b^2)\left(d^2-l_j^2/4\right)}}\right) \end{aligned} \tag{14}$$

where j equals 1 or 2. Then the coordinates of c_{11} and c_{12} in $\{O_{Bi}\}$ can be calculated easily and denoted as ${}^{O_{B1}}\boldsymbol{c}_{11}$ and ${}^{O_{B1}}\boldsymbol{c}_{12}$. Similarly, the coordinates of c_{i1} and c_{i2} in $\{O_{Bi}\}$ can be obtained. Due to the location of the elastic ring is attached to the middle creases of the module, only the changing lengths of $c_{11}c_{32}$, $c_{12}c_{21}$ and $c_{22}c_{31}$ will generate the pulling force from the elastic ring. Let the lengths of $c_{11}c_{32}$, $c_{12}c_{21}$ and $c_{22}c_{31}$ be denoted as d_{12}, d_{23} and d_{31}, respectively. Using the homogeneous transformation matrix in (13), the coordinates of c_{i1} and c_{i2} described in $\{O_{Bi}\}$ can be transformed into the base coordinate system $\{O_b\}$, and these distances can be calculated. Taking d_{12} as an example:

$$d_{12} = \left\| {}^{O_b}\boldsymbol{T}_{O_{B1}}^{O_{B1}}\boldsymbol{c}_{11} - {}^{O_b}\boldsymbol{T}_{O_{B3}}^{O_{B3}}\boldsymbol{c}_{32} \right\|_2 \tag{15}$$

From (15), d_{12} not only depends on actuation cable l_1, but also depends on the other two actuation cables l_2 and l_3, and it will increase as any length of the actuation cables decreases. This means when the proposed robot deviates from its initial configuration where all cables have the maximum length, the elastic rings will produce elastic force because of the increase of d_{12}, which can be used for configuration maintenance and self-deployment.

V. Experiments

A. Control System Setup

In the control system of the robot, three DC motors with encoders and decelerators (30:1) are utilized. The control board of the motor is STM32F407. To minimize actuation errors, a double closed-loop PID of speed and position is implemented.

B. Comparison Experiments

Firstly, the continuum robot was deployed to its maximum extent and then contracted to its minimum height ten times, considering the influence of gravity. The average maximum height was 185 mm, while the minimum height was 42 mm, resulting in a deploy/fold ratio of 4.4, which overtakes most of the related studies (in [19] it is 2.25, in [26] it is 2.875, and in [28] it is 1.70).

Next, elastic rings and synchronism mechanism were disassembled from the proposed robot respectively, and compared to the proposed robot, as shown in Fig. 6. It is clear to see that the elastic rings can provide elastic force for maintaining the configuration. If there are no angle limitations in the facets of each module, facets in each chain of the module will contact each other under the elastic force from elastic rings. The proposed slider-crank mechanisms can limit maximum facet angles by limiting the traveling distance of each slider. Therefore, without the aid of the synchronism mechanism, a singularity will occur in each module.

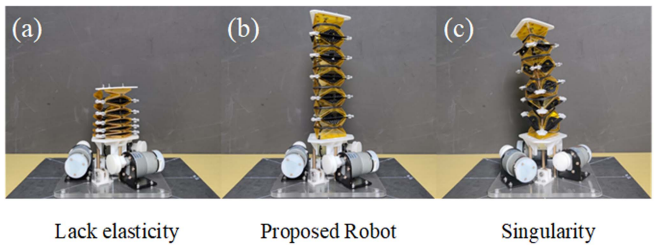

Fig. 6. Structure comparison. (a) Without elastic rings. (b) With both elastic rings and synchronism mechanisms. (c) Without synchronism mechanisms.

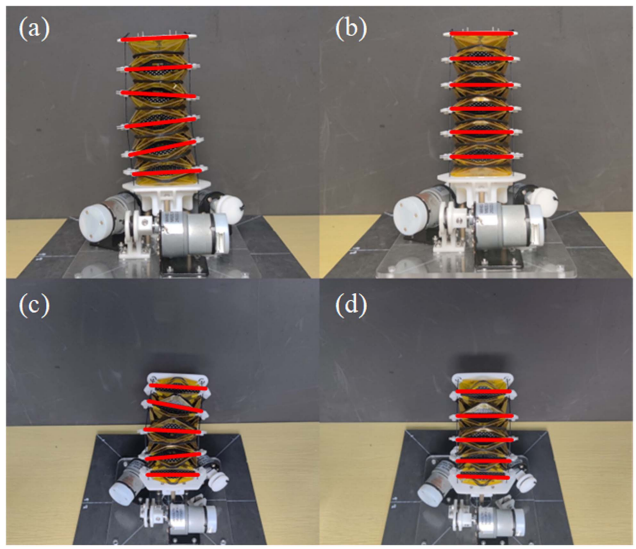

Fig. 7. Motion comparison. (a) Contraction without synchronism mechanism. (b) Contraction with synchronism mechanism. (c) Bending without synchronism mechanism. (d) Bending with synchronism mechanism.

To demonstrate the function of the synchronism mechanism, a simple contraction motion and a bending motion were tested, as illustrated in Fig. 7. These two configurations were observed from two different perspectives to better show the motion synchronism between each module. From the result, it is evident that there is an improvement in motion synchronicity, with all modules maintaining a relatively consistent configuration. This improvement is beneficial for motion certainty and control.

C. Motion Accuracy and Trajectory Tracking Experiments

To demonstrate the positioning capability and validate the proposed forward kinematic model, position errors for 9 configurations were tested randomly, with the initial length of each cable being 190 mm. These configurations were divided into three sets based on the range of length variation, and each configuration was measured three times. The average error for each configuration is shown in Fig. 8(a). As the length variation range increases, the position error tends to decrease due to the increase of elastic force. The position errors are higher near the initial state because of the influence of gravity. Considering the gravity

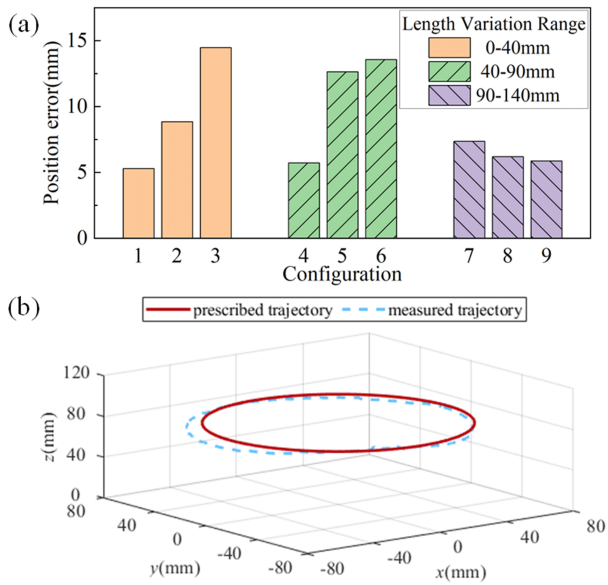

Fig. 8. Motion accuracy and trajectory tracking. (a) Average position errors of nine configurations in different length variation ranges. (b) Trajectory tracking.

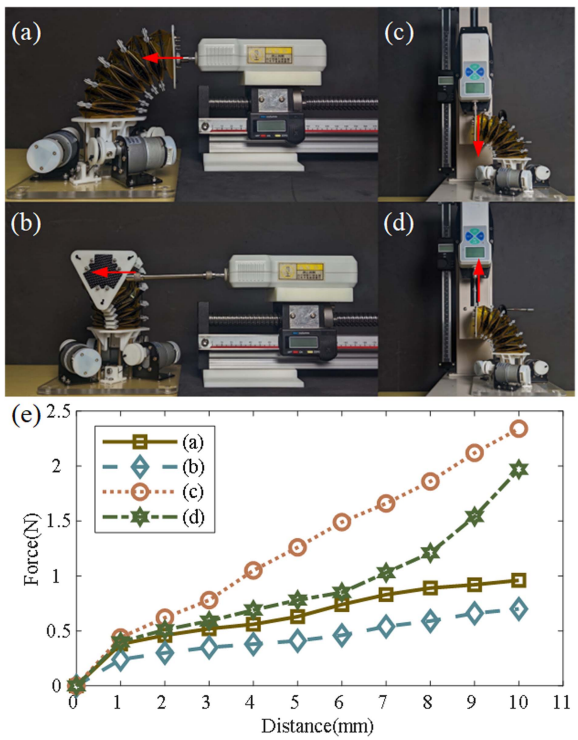

Fig. 9. Stiffness experiment. (a) Test direction a. (b) Test direction b. (c) Test direction c. (d) Test direction d. (e) Test results.

error and other potential errors from the measurement system and driving system, the results can confirm the correctness of the proposed forward kinematics.

To demonstrate the motion capability and validate the proposed inverse kinematic model, a circular trajectory with a radius of 65 mm was prescribed to evaluate its tracking performance, as shown in Fig. 8(b). The measured trajectory exhibits a relatively large deviation from the prescribed trajectory in some configurations, which may be caused by inaccurate cable lengths, error accumulation from the reel, and the influence of gravity. Overall, the average error in trajectory tracking is 5.89 mm. This confirms the proposed inverse kinematic model.

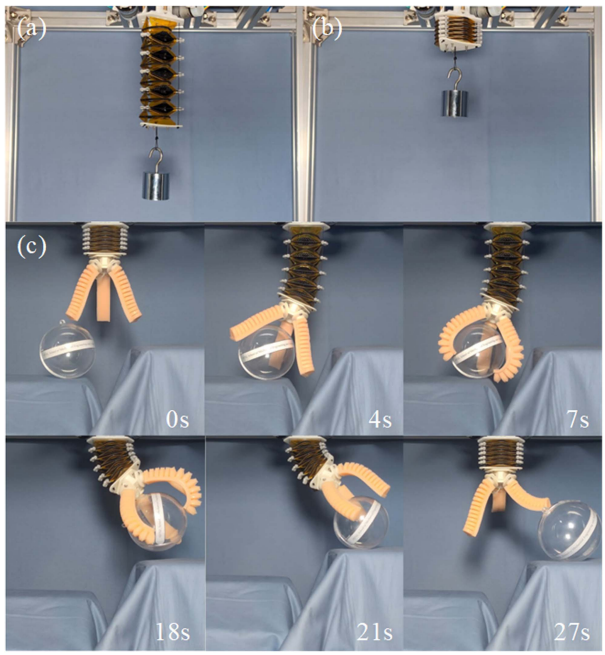

Fig. 10. Load and application experiments. (a)-(b) Load capacity. (c) Move an object from a place to a different height.

D. Stiffness Experiments

Without loss of generality, we measured the reaction force and the moving distance of the robot in a bending configuration from four different directions, as shown in Fig. 9. The results indicate that the stiffness in directions (c) and (d) is higher than the stiffness measured in directions (a) and (b). The different stiffness in these four experiments is mainly caused by the direction of the applying force and the consequent kinematics. On the other hand, manufacturing errors cause small gaps, then the proposed slider-crank mechanism cannot fully constrain the mobility, which means that the robot is still underactuated and easy to be disturbed.

E. Load Capacity and Grasping Experiments

To demonstrate the load capacity, we hung the proposed continuum robot upside down in a fully deployed configuration first, then lifted a load of 500 g to test the load capacity, as shown in Fig. 10(a) and (b). Because the load capacity of this robot only depends on the pulling force of the driving cables of its motors, it is easy to lift any load within the load capacity of the three driving motors. Only the contraction direction is used for loading objects, the bending and deploying directions are only used for end-effector positioning, so we only test the load capacity in the contraction direction.

To explore potential applications, we integrated a conventional pneumatic soft hand, weighing 111.7 g, at the end of the robot. A sphere object was selected for the grasping experiment and the motion sequence is depicted in Fig. 10(c). The result confirms that the proposed continuum robot can reach a far location through deployment motion and transport an object weighing approximately 1.86 times its weight. The detailed process of grasping can be found in supplementary media.

VI. Conclusion

In this letter, we presented a novel 3 DOFs deployable continuum robot using elastic Yoshimura kirigami-origami, demonstrating configuration maintenance capability through the utilization of the active cables and passive elastic deformation of the kirigami-origami. Both forward and inverse kinematic models were created, and the self-deployment principle of the proposed robot using elastic rings was analyzed. A physical prototype has been fabricated, and experiments have been conducted to show its performance. The experiments showed that the proposed robot can achieve a perfect deploy/fold ratio of 4.4, and the synchronism mechanism plays an important role in avoiding singularity and improving synchronous motion of each module. Experiments also validated the proposed kinematic models and demonstrated high load capacity for the proposed robot. In future work, the motion accuracy of the robot may be improved through high-precision mechanical design and closed-loop control.

References

[1] J. L. C. Santiago, I. D. Walker, and I. S. Godage, "Continuum robots for space applications based on layer-jamming scales with stiffening capability," in *Proc. IEEE Aerosp. Conf*., 2015, pp. 1–13.

[2] A. P. Rubio et al.., "Modular morphing lattices for large-scale underwater continuum robotic structures," *Soft Robot.*, vol. 10, no. 4, pp. 724–736, Aug. 2023.

[3] Y. Kong, S. Song, N. Zhang, J. Wang, and B. Li, "Design and kinematic modeling of in-situ torsionally-steerable flexible surgical robots," *IEEE Robot. Automat. Lett.*, vol. 7, no. 2, pp. 1864–1871, Apr. 2022.

[4] J. Zhang et al.., "Versatile like a seahorse tail: A bio-inspired programmable continuum robot for conformal grasping," *Adv. Intell. Syst.*, vol. 4, no. 11, Oct. 2022, Art. no. 2200263.

[5] S. Phodapol, A. Harnkhamen, N. Asawalertsak, S. N. Gorb, and P. Manoonpong, "Insect tarsus-inspired compliant robotic gripper with soft adhesive pads for versatile and stable object grasping," *IEEE Robot. Automat. Lett.*, vol. 8, no. 5, pp. 2486–2493, May 2023.

[6] X. Huang, J. Zou, and G. Gu, "Kinematic modeling and control of variable curvature soft continuum robots," *IEEE/Amer. Soc. Mech. Engineers Trans. Mechatron.*, vol. 26, no. 6, pp. 3175–3185, Dec. 2021.

[7] K. Ma, X. Chen, J. Zhang, Z. Xie, J. Wu, and J. Zhang, "Inspired by physical intelligence of an elephant trunk: Biomimetic soft robot with pre-programmable localized stiffness," *IEEE Robot. Automat. Lett.*, vol. 8, no. 5, pp. 2898–2905, May 2023.

[8] A. Stilli, E. Kolokotronis, J. Fraś, A. Ataka, K. Althoefer, and H. A. Wurdemann, "Static kinematics for an antagonistically actuated robot based on a beam-mechanics-based model," in *Proc. IEEE/RSJ Int. Conf. Intell.*, 2018, pp. 6959–6964.

[9] H. Wang, Z. Zhou, X. Yang, and X. Zhang, "A switchable rigid-continuum robot arm: Design and testing," in *Proc. IEEE Int. Conf. Robot. Automat.*, 2022, pp. 5162–5169.

[10] J. Cai, Q. Zhong, X. Zhang, K. Wang, Q. Zhang, and J. Feng, "Mobility and kinematic bifurcation analysis of origami plate structures," *J. Mechanisms Robot.*, vol. 15, no. 6, Jan. 2023, Art. no. 061015.

[11] M. Meloni et al.., "Engineering origami: A comprehensive review of recent applications, design methods, and tools," *Adv. Sci.*, vol. 8, no. 13, May 2021, Art. no. 2000636.

[12] Q. Zhang, H. Fang, and J. Xu, "Yoshimura-origami based earthworm-like robot with 3-dimensional locomotion capability," *Front. Robot. AI*, vol. 8, Aug. 2021, Art. no. 738214.

[13] Q. Ze et al.., "Soft robotic origami crawler," *Sci. Adv.*, vol. 8, no. 13, Mar. 2022, Art. no. eabm7834, doi: 10.1126/sciadv.abm7834.

[14] J. Huang et al.., "Modular origami soft robot with the perception of interaction force and body configuration," *Adv. Intell. Syst.*, vol. 4, no. 9, Jun. 2022, Art. no. 2200081.

[15] J.-G. Lee and H. Rodrigue, "Origami-based vacuum pneumatic artificial muscles with large contraction ratios," *Soft Robot.*, vol. 6, no. 1, pp. 109–117, Feb. 2019.

[16] M. Meloni, Q. Zhang, J. Cai, and D. S.-H. Lee, "Origami-based adaptive facade for reducing reflected solar radiation in outdoor urban environments," *Sustain. Cities Soc.*, vol. 97, Oct. 2023, Art. no. 104740.

[17] S. Wang, P. Yan, H. Huang, N. Zhang, and B. Li, "Inflatable metamorphic origami," *Research*, vol. 6, May 2023, Art. no. 0133.

[18] Y. Xu, Q. Peyron, J. Kim, and J. Burgner-Kahrs, "Design of lightweight and extensible tendon-driven continuum robots using origami patterns," in *Proc. IEEE Int. Conf. Soft Robot.*, 2021, pp. 308–314.

[19] J. Santoso and C. D. Onal, "An origami continuum robot capable of precise motion through torsionally stiff body and smooth inverse kinematics," *Soft Robot.*, vol. 8, no. 4, pp. 371–386, Aug. 2021.

[20] X. Wei et al.., "Annelid-inspired high-elongation origami robot using partial material removal," *Bioinspiration Biomimetics*, vol. 18, no. 1, Dec. 2022, Art. no. 016013.

[21] H. Liang, G. Hao, O. Z. Olszewski, Z. Jiang, and K. Zhang, "Design of a foldable origami mechanism with helical motion inspired by the Resch Triangular Tessellation," *Mechanism Mach. Theory*, vol. 179, Jan. 2023, Art. no. 105101.

[22] J. Zhang, J. Chen, Y. Dang, and J. Han, "Design and analysis of a Yoshimura continuum actuator," in *Proc. Int. Conf. Mechatron. Mach. Vis. Pract.*, 2022, pp. 1–6.

[23] M. Salerno, K. Zhang, A. Menciassi, and J. S. Dai, "A vovel 4-DOF origami grasper with an SMA-actuation system for minimally invasive surgery," *IEEE Trans. Robot.*, vol. 32, no. 3, pp. 484–498, Jun. 2016.

[24] M. A. Robertson, O. C. Kara, and J. Paik, "Soft pneumatic actuator-driven origami-inspired modular robotic 'pneumagami," *Int. J. Robot. Res.*, vol. 40, no. 1, pp. 72–85, Mar. 2020.

[25] S. Liu et al.., "Otariidae-inspired soft-robotic supernumerary flippers by fabric kirigami and origami," *IEEE/Amer. Soc. Mech. Engineers Trans. Mechatron.*, vol. 26, no. 5, pp. 2747–2757, Oct. 2021.

[26] Z. Zhang, S. Tang, W. Fan, Y. Xun, H. Wang, and G. Chen, "Design and analysis of hybrid-driven origami continuum robots with extensible and stiffness-tunable sections," *Mechanism Mach. Theory*, vol. 169, Mar. 2022, Art. no. 104607.

[27] Y. Yu, L. Qiu, S. Dai, C. Li, and D. Wang, "Creating a flexible continuum robot using origami and mortise-tenon structure," *Mechanism Mach. Theory*, vol. 176, Oct. 2022, Art. no. 104978.

[28] Z. Zhuang et al.., "Design and control of SLPM-based extensible continuum arm," *J. Mechanisms Robot.*, vol. 14, no. 6, Dec. 2022, Art. no. 061003.

[29] K. Zhang, Y. Fang, H. Fang, and J. S. Dai, "Geometry and constraint analysis of the three-spherical kinematic chain based parallel mechanism," *J. Mechanisms Robot.*, vol. 2, no. 3, Jul. 2010, Art. no. 031014.

[30] K. Zhang, C. Qiu, and J. S. Dai, "An extensible continuum robot with integrated origami parallel modules," *J. Mechanisms Robot.*, vol. 8, no. 3, Mar. 2016, Art. no. 031010.